Authors' last submission before acceptance.
Pubslished in Computers and Fluids,
Vol. 228, 15 Oct. 2021, Article No. 105054
https://doi.org/10.1016/j.compfluid.2021.105054

Large-eddy simulations of the flow over a semi-circular cylinder at Re = 50000

Dmitry A. Lysenko[a,*], Mark Donskov[a], Ivar S. Ertesvåg[b]

[a] *3DM Simtek AS, Risabergvegen 88, N0–4056, Tananger, Norway*
[b] *Department of Energy and Process Engineering, NTNU Norwegian University of Science and Technology, Kolbjørn Hejes vei 1B, NO–7491, Trondheim, Norway*

Abstract

Large-eddy simulations (LES) of the flow over a semi-circular cylinder at a diameter-based Reynolds number 50000 and zero angle of attack are presented. In comparison with the prominent benchmark flows past circular and square cylinders, this test problem has been less investigated in the literature from both numerical and experimental perspectives. Also, this case can be even more challenging for validation and verification of the computational codes due to a negative lift force, which characterizes this flow regime. A standard numerical platform based on a second-order finite volume method and the k-equation eddy viscosity subgrid scale model and its dynamic version, implemented in the OpenFOAM CFD toolbox, is used for the present LES. A detailed spectral analysis is provided to examine dynamics of the vortex shedding and shear layer instabilities. The moderate Reynolds number is chosen in order to replicate experimental data, which is limited to integral flow parameters like the lift, drag and pressure coefficients and a Strouhal number. The numerical and experimental data available for the flows over the circular and square cylinders at the Reynolds number $20000-50000$ are used for qualitative assessment of the present results. Similarity of the turbulent wakes between the circular, square and semi-circular cylinders are discussed and compared both, for the integral

*Corresponding author
Email addresses: dmitry.lysenko@3dmsimtek.no (Dmitry A. Lysenko), ivar.s.ertesvag@ntnu.no (Ivar S. Ertesvåg)

flow parameters and high order statistics as well. Overall, present simulations provide reasonable agreement with available measurements and numerical calculations. Consistency and satisfactory agreement with the previous numerical and experimental results obtained for the circular and square cylinders are shown as well.
Keywords: large-eddy simulation, semi-circular cylinder, turbulent separated flows, vortex shedding, bluff body aerodynamics

1. Introduction

The turbulent, separated flows past bluff-bodied play a significant role in external aerodynamic applications and have been studied intensively by different experimental and numerical methods. The circular and square cylinders are the most prominent configurations, and have been under research almost during the century. The work by Thom [1], who performed the first viscous simulation of the flow over a circular cylinder, dated to 1933, can be considered as the pioneer paper, available in the literature. From this prospect the flow past a semi-circular cylinder is less studied configuration both in terms of the physical measurements and numerical analysis. The goal of this paper is to provide numerical simulations of the turbulent flow past the semi-circular cylinder using a large-eddy simulation model. The open source CFD toolbox OpenFOAM [2] was utilized for this purpose.

Previously, the large-eddy simulation technique was validated against the flow past a circular cylinder at the Reynolds numbers, Re = 3900 [3] and Re = 20000 [4]. The Reynolds number is defined as $\mathrm{Re} = \rho_\infty U_\infty D/\mu$, where U_∞ and ρ_∞ are the free-stream velocity and mass density, respectively, D is the diameter of the cylinder and μ represents the dynamic viscosity. Lately, both inert and reactive flows over a triangular cylinder at $\mathrm{Re} = 45000 - 47000$ using unsteady Reynolds-averaged Navier-Stokes (URANS), LES and Scale-Adaptive simulations (SAS) have been investigated [5]. The global descriptions of LES, SAS and RANS/URANS indicated a clear interrelation between these three ap-

proaches for simulating reactive or non-reactive turbulent flows [5]. In general, reasonable consistency was found for these different approaches as well as satisfactory agreement between numerical simulations and measurements. However, the most accurate results were reached using the large-eddy simulations.

A parallel aim is to develop a concept of a bluff-body vehicle with an integrated active flow control (AFC hereafter) system, based on the vortex cells. This configuration is promising for the study of the aerodynamic shape of airframes with integrated active flow control systems for flying vehicles. As an example, the EKIP flying vehicle [6] represents a thick flying airfoil whose thickness comprises to 37.5%. A flow without separation around the EKIP profile can be organized by development of AFC to organize a suction of air from the pressure side of the object.

Therefore, the flow over the semi-circular cylinder (HC hereafter) at the Reynolds number Re = 50000 can provide a fundamental basis as a starting point for the further AFC development. On one hand, the availability of experimental data [7], [8], was one of the reasons why this particular Reynolds number was replicated. On the other hand, there is practical interest to this problem as it can be seen as the flow past a thick airfoil mounted at the zero angle of attack. In addition, HC can be treated as a limiting case between the circular and square cylinders (CC and SC hereafter). However, HC has a unique feature which is the abnormal behavior of the lift coefficient, especially at the zero angle of attack, which makes this test even more attractive and challenging for validation and verification of the modern computational fluid dynamics (CFD) codes compared to CC and SC cases.

In the present work, we utilized the standard numerical platform (the second-order finite-volume method and Yoshizawa and Smagorinsky sub-grid scale models), implemented in the OpenFOAM code. This numerical approach has been validated in details for the bluff-body flows during the last decade (e.g., [3], [4], [9], [10], [11], [12]) and can be recommended to simulate the turbulent separated flows.

The differences between the present LES, available URANS [8], [13] and

experimental results were discussed [7], [8]. Furthermore, we provided a detailed analysis and comparison of the available numerical (LES and direct numerical simulations, DNS) and experimental data for the flows past CC ([14], [15], [16], [17], [18], [4], [19]) and SC ([20], [21], [22], [23], [9], [24], [11], [25]) to compensate the limitation of HC experimental data to the integral flow parameters only.

Similarity of the turbulent wakes downstream of these bluff-body configurations are presented. The integral aerodynamic characteristics and pressure distributions for HC, SC and CC are compared. Here, the Reynolds numbers were limited to the range, $20000 \leq \mathrm{Re} \leq 50000$, respectively,

Finally, the key factors leading to deviations and discrepancies between the numerical and experimental results are discussed. In the same spirit as Trias et al. [24], who have noticed a great dispersion of the bulk quantities obtained for the SC case, the similar situation was observed for the CC and HC cases. Also it it important to note that only limited, experimental data (lift and drag coefficients, the Strouhal number and distribution of the pressure coefficient along the cylinder) are available for HC for the strong LES validation.

The paper is divided into five main sections. The first section of the paper describes the mathematical modeling and numerical aspects. Then, a general description of the test case is given. Finally, computational results are presented, results are analyzed and discussed, and on the top of that conclusions are drawn.

2. Brief description of mathematical modeling numerical aspects

In order to be consistent with authors' previous results [3], [4],[5], the compressible flow and related numerical setup were considered despite of the fact that the actual Mach number was close to the incompressible limit.

2.1. Mathematical modeling

The Favre filtered balance equations of mass, momentum and energy were solved:

$$\frac{\partial \bar{\rho}}{\partial t} + \frac{\partial \bar{\rho} \widetilde{\mathbf{u}}_j}{\partial x_j} = 0, \tag{1}$$

$$\frac{\partial \bar{\rho}\widetilde{\mathbf{u}}_i}{\partial t} + \frac{\partial \bar{\rho}\widetilde{\mathbf{u}}_i\widetilde{\mathbf{u}}_j}{\partial x_j} + \frac{\partial \bar{p}}{\partial x_i} - \frac{\partial \check{\sigma}_{ji}}{\partial x_j} = -\frac{\partial \tau_{ij}}{\partial x_j} \tag{2}$$

$$\frac{\partial \bar{\rho}\widetilde{h}}{\partial t} + \frac{\partial \bar{\rho}\widetilde{h}\widetilde{\mathbf{u}}_j}{\partial x_j} - \frac{\partial \bar{p}}{\partial t} - \widetilde{\mathbf{u}}_j\frac{\partial \bar{p}}{\partial x_j} + \frac{\partial \check{q}_j}{\partial x_j} - \check{\sigma}_{ji}\widetilde{S}_{ij} = -C_v\frac{\partial Q_j}{\partial x_j}. \tag{3}$$

Here ρ, p and $\mathbf{u}$ are density, pressure and velocity, respectively. $h = \varepsilon + p/\rho$ is the enthalpy per unit mass and ε is the internal energy per unit mass and T is temperature. The $(\bar{\cdot})$, $(\widetilde{\cdot})$ and $(\check{\cdot})$ marks are denoting the Reynolds-averaging, filtering Favre-averaging and filtering operators.

The diffusive fluxes were set accordingly

$$\check{q}_j = -\kappa(\widetilde{T})\frac{\partial \widetilde{T}}{\partial x_i}, \tag{4}$$

$$\check{\sigma}_{ij} = 2\mu(\widetilde{T})\left(\widetilde{S}_{ij} - \frac{1}{3}\delta_{ij}\widetilde{S}_{kk}\right), \tag{5}$$

where $\widetilde{S}_{ij}$ is the rate-of-strain tensor

$$\widetilde{S}_{ij} = \frac{1}{2}\left(\frac{\partial \widetilde{\mathbf{u}}_i}{\partial x_j} + \frac{\partial \widetilde{\mathbf{u}}_j}{\partial x_i}\right), \tag{6}$$

μ is the viscosity (calculated according to the Sutherland's law) and κ represents conductivity. Finally, the filtered equation of state was used to close the system of equations

$$\bar{p} = \bar{\rho}R\widetilde{T}. \tag{7}$$

The compressible flow was calculated at the particular Mach number, $\mathrm{M} = U_\infty/c_\infty = 0.03$, where c_∞ is the speed of sound in the free stream. The sub-grid scales incompressibility hypothesis was assumed since the Mach number was sufficiently low [26]. Thus, the SGS stress τ_{ij} and heat flux Q_j were calculated as

$$\tau_{ij} = \bar{\rho}\left(\widetilde{\mathbf{u}_i\mathbf{u}_j} - \widetilde{\mathbf{u}}_i\widetilde{\mathbf{u}}_j\right), \tag{8}$$

$$Q_j = \bar{\rho}\left(\widetilde{\mathbf{u}_j T} - \widetilde{\mathbf{u}}_j\widetilde{T}\right). \tag{9}$$

The k-equation eddy viscosity sub-grid scale model [27] (hereafter, TKE) and its dynamic version (hereafter, dTKE) were utilized for the closure problem. Both models were based on the SGS kinetic energy $\tilde{k} = \frac{1}{2}\left(\widetilde{\mathbf{u}\cdot\mathbf{u}} - \widetilde{\mathbf{u}}\cdot\widetilde{\mathbf{u}}\right)$. The

following assumptions for the SGS density weighted stress tensor $\mathbf{B}$ and the filtered deviatoric part of the rate of strain tensor $\widetilde{\mathbf{D}}_D$ were used:

$$\mathbf{B} = \frac{2}{3}\bar{\rho}\tilde{k}\mathbf{I} - 2\mu_B\widetilde{\mathbf{D}}_D, \tag{10}$$

$$\widetilde{\mathbf{D}}_D = \left[\widetilde{\mathbf{D}} - \frac{1}{3}\left(\mathrm{tr}\widetilde{\mathbf{D}}\right)\mathbf{I}\right], \tag{11}$$

$$\widetilde{\mathbf{D}} = \frac{1}{2}\left(\mathrm{grad}\ \widetilde{\mathbf{u}} + \mathrm{grad}\ \widetilde{\mathbf{u}}^{\mathrm{T}}\right), \tag{12}$$

$$\mu_B = c_k\overline{\rho}\sqrt{\tilde{k}}\Delta. \tag{13}$$

Here $\mathbf{I}$ is the unit tensor, μ_B the SGS viscosity and Δ the top-hat filter with a length estimated as the cubic root of the control volume. The subgrid kinetic energy $\tilde{k}$ was estimated by solving a separately modeled transport equation of the form,

$$\frac{\partial}{\partial t}\left(\bar{\rho}\tilde{k}\right) + \frac{\partial}{\partial x_j}\left(\bar{\rho}\widetilde{\mathbf{u}}_j\tilde{k}\right) = F_p + F_d - F_\epsilon, \tag{14}$$

$$F_p = -\mathbf{B}\cdot\widetilde{\mathbf{D}}, \tag{15}$$

$$F_d = \frac{\partial}{\partial x_j}\left(\left(\mu_B + \mu\right)\frac{\partial\tilde{k}}{\partial x_j}\right), \tag{16}$$

$$F_\epsilon = c_\epsilon\ \bar{\rho}\ \tilde{k}^{3/2}/\Delta, \tag{17}$$

where F_p is production, F_d diffusion and F_ϵ dissipation terms, respectively, and $c_k = 0.07$, $c_\epsilon = 1.048$ are model coefficients [28]. The Germano identity $\mathbf{L}$ with another filter kernel of width $\overline{\Delta} = 2\Delta$ was used to derive the dynamic version [29].

2.2. Numerical method

The present simulations were carried out using the OpenFOAM v6.0 [2] code. The finite-volume method based on the the standard pressure–velocity coupling methodology and the PIMPLE algorithm [10], which is a variation of the PISO (pressure implicit with splitting of operators) method [30], was used to solve the governing equations. The system of linear algebraic equations were

computed based on a smooth solver (with a symmetrical Gauss-Seidel smoother) with a local accuracy of 10^{-7} for all dependent variables except pressure. The last one was calculated using the Geometric agglomerated algebraic multigrid solver(GAMG) with the Gauss-Seidel smoother and a local accuracy of 10^{-7}. The LUST (Linear-Upwind Stabilized Transport) divergence scheme with 0.25 linear-upwind and 0.75 linear weights was used for the velocity and energy fields to avoid artificial pressure oscillations [31]. All other terms were approximated by the total variation diminishing (TVD) [32] scheme. The BDF-2 method [26], accompanied by the dynamic adjustable time stepping technique (to keep a local Courant number less than 0.4), was applied for time integration.

2.3. High performance computing

The present simulations were carried out at the Vilje high performance computing (HPC) facility, which is a distributed memory system that consists of 1440 nodes interconnected with a high-bandwidth low-latency switch network (FDR Infiniband). Each node has two 8-core Intel Sandy Bridge (2.6 GHz) and 32 GB memory.

Figure 1 displays results of the performance test obtained for the investigated problem for several grid resolutions ($13M$, $25M$ and $39M$, where the number indicates the amount of finite-volume cells) using the number of MPI (message passing interface) processes up to $p = 2048$. Both the strong scaling, $S_p = T_p/T_1$, and the parallel efficiency, $E_p = S_p/p$ (the weak scaling), where investigated. Here, T_1 and T_p are computing time on a single node and computing time on multiple nodes. It is important to note that T_1 for the $13M$ grid was obtained on the single node. T_1 for the $25M$ and $39M$ grids were derived on two and three nodes, respectively, due to the large problem size and the 32 GB memory limitation for the single node. Also, all low-level I/O operations were disabled during the present scalability test. OpenFOAM demonstrated quite good strong and week scaling averaging efficiency of approximately 70% of an ideal for $p = 1024$, which is very satisfactory for the state-of-the-art implicit pressure-based solvers.

In the present study $256-512$ processes in parallel were used, witch provides the typical calculation time for one time step between $1-2$ s, resulted in the total (effective) simulation time per run around two-three weeks.

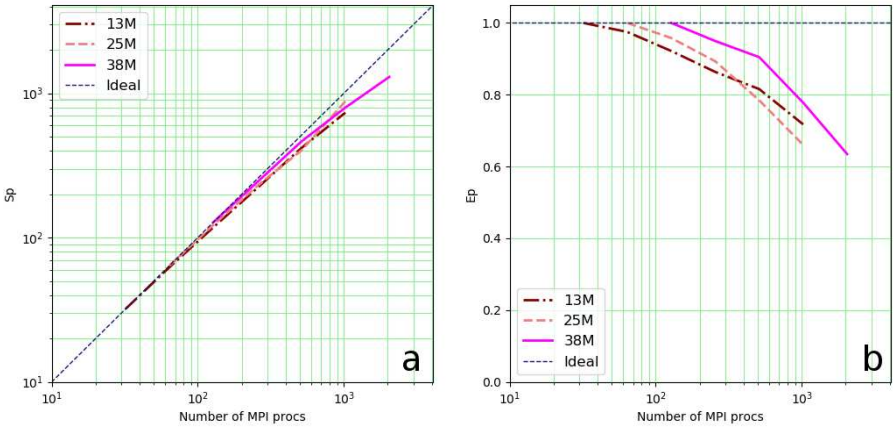

Figure 1: Vilje HPC parallel performance study: strong (a) and week (b) scaling results for the flow past a semicircular cylinder at $\mathrm{Re} = 50000$ using different grid sizes

3. Problem formulation

3.1. Flow physics and topology of the flow over a semi-circular cylinder

The Reynolds number based on the diameter of the semi-circular cylinder and free-stream velocity was set to $\mathrm{Re} = 50000$ and the Mach number to $\mathrm{M} = 0.03$. Similar to the circular cylinder, the key features of the flow mechanics for the sub-critical flow regime are the laminar boundary layers, separated shear layers, near- and far-wakes and the flow instabilities that provide complex, nonlinear interaction between them (Figure 2). Two types of instabilities dominate the wake: the vortex shedding (Bénard/von Kármán instability, BVK hereafter) and the Kelvin–Helmholtz instability (KH hereafter) of the separated shear layer.

Under some assumptions, the flow dynamics can be considered as a superposition of the two simultaneous processes. First, the boundary layer from the

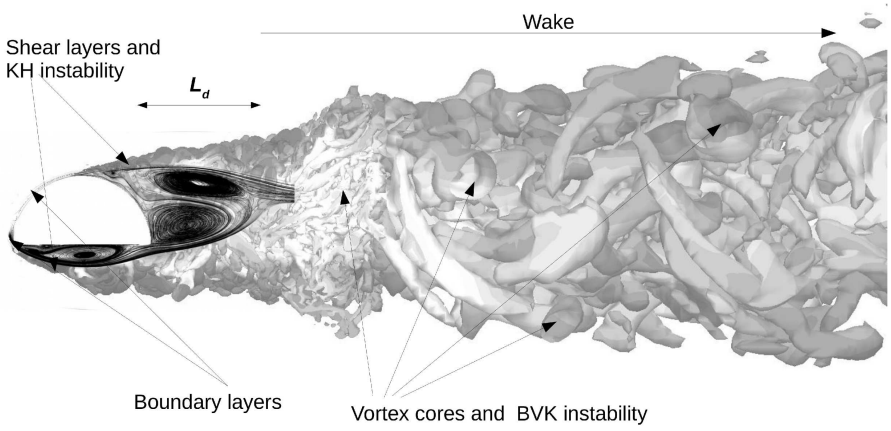

Figure 2: Key flow features in an bluff-body flow, with superposition of the instantaneous topology and time-averaged streamlines. Mean and instantaneous visualization are obtained from the present study

pressure (upper) side of the semi-circular cylinder is separated, rolled up and transformed into a large-scale vortex, which moves away from the obstacle and forms the large rarefaction zone downstream the bluff-body. At the same time, the boundary layer is separated from the leading edge of the obstacle from its suction side and rolled up to the large-scale vortex, which is convected by the free-stream flow towards the trailing edge. While moving along the suction side, the vortex core is growing. By reaching the trailing edge, this vortex is grabbed into the rarefaction zone, merged with the large scale structures formed downstream of the cylinder and moved downstream to the wake. It should be noted that we defined the pressure and suctions sides of the semi-circular cylinder similar to airfoils terminology.

In the present study the recirculation length of the detached reversed bubble L_d is defined to the distance between the base of the cylinder and the location of mean stream-wise velocity sign change along the axial direction at $y/D = 0.25$.

3.2. Boundary and initial conditions

The inflow velocity, temperature and turbulence properties were specified to satisfy the free-stream Reynolds and Mach number conditions.

The fluid medium was treated as compressible air (assuming the ideal gas law with the ratio of specific heats set to $\phi = 1.4$). The Prandtl number was set to 0.72. The dynamic viscosity and the thermal conductivity were defined to be constant values. Some perturbations of 5% magnitude was added to the inlet velocity using a simple synthetic generator based on a white noise random fluctuation superposition. The inlet value for the turbulence kinetic energy was set to 0.2% to provide computational stability of LES calculations. A zero-gradient pressure boundary was applied for all inflow boundaries, while the pressure at the outlet was specified to 101325 Pa. A non-slipping condition for velocity was applied to the cylinder's surface. The turbulence kinetic energy were set to zero at the surface of bluff-body. Symmetry planes were imposed at the lateral boundaries. Boundary conditions for temperature at solid walls were treated according to the zero-gradient assumption. The inflow conditions were used as initial conditions.

3.3. Computational domain and grids

The diameter of the semi-circular cylinder, D, was taken as a characteristic size so that all the linear sizes were made dimensionless by it. The center of the Cartesian x,y coordinates was located in the center of the semi-circular base. Two grids were used for the present LES.

3.3.1. The low-resolution grid

The computational domain of the first grid had dimensions of $30D \times 20D \times 10D$ in x, y and z directions, respectively. As a starting point, the computational box had a size of $60 \times 40 \times 20$ nodes. This mesh was sequentially refined by three levels with a factor of $2 \times 2 \times 2$ in regions from $y/D = -4$ to $y/D = 4$, $y/D = -2.25$ to $y/D = 2.25$ and $y/D = -1.9$ to $y/D = 1.9$. The next refinement level with the same factor was applied to the cylinder area with the radius of 1.75 located at the center of the Cartesian coordinates. The final level was added to the box extended from $x/D = -1$ to $x/D = 2$ and $y/D = -1$ to $y/D = 1$. All adapted regions fully covered the span-wise direction. The viscous

boundary layer was attached to the obstacle. The corners of the semi-circular cylinder were slightly rounded with the the radius of curvature $r/D = 0.025$. The nearest cell height (h_{1st}) was set to $7.5{\times}10^{-5} < 0.1/\mathrm{Re}^{0.5} = 4.5{\times}10^{-4}$. The growth factor and the total number of rows were set to 1.04 and 27, respectively. The total number of cells was 11.02 million. Hereafter, this grid has the label H1.

3.3.2. The high-resolution grid

Figure 3 presents some details of the second LES grid (labeled H2). This grid was designed in the same spirit as H1, except the resolution of the starting computational box was increased by factor of 1.5 leading to an initial size of $90\times 60\times 30$. The nearest cell height (h_{1st}), the growth factor and the total number of rows of the boundary layer were set to 5×10^{-5}, 1.04 and 40, respectively. The total number of cells was 24.57 million. The present LES grid resolution seemed to be sufficient compared to that used in previous test for the flow past a circular [9] and a square cylinders [11].

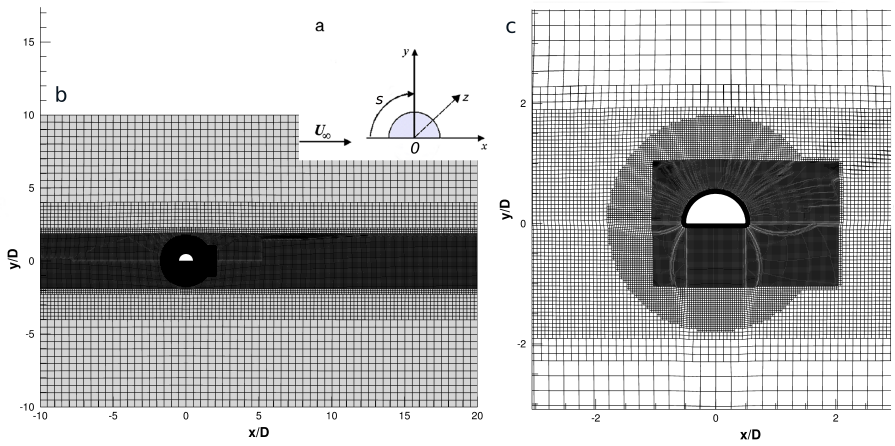

Figure 3: The general view of the H2 grid and computational domain (a), the description of the grid (b) and zoom of the grid at the vicinity of the bluff-body (c). x, y and z are the domain coordinates in stream-wise, transverse and span-wise directions. s is the the circumferential coordinate, normalized by the total length of the semi-circular cylinder ($\pi D/2 + D$)

3.3.3. Span-wise resolution

It should be noted that the span resolution of the present grids were $\Delta z/D = 0.018$ and $\Delta z/D = 0.012$ for H1 and H2, respectively. Recently, Cao et al.[25] provided a detailed analysis of the span resolution requirements for the flow over the square cylinder at Re = 22000. They showed that the requirement $\Delta z/D = 0.04$ was sufficient to predict the mean and root-mean-square values of aerodynamic forces, velocity field and small-scale turbulent motions in the wake. However, $\Delta z/D \leq 0.02$ was suggested to predict accurately the shear layer behaviors and the laminar-turbulent transitional process, which characterized by the wide spectrum of the coherent structures, including stream-wise and span-wise vortices.

In practice, it is reasonable to assume that the span-wise wavelength of the stream-wise vortices is scaling as the square root of the Reynolds number [33]. According to Williamson et al. [33], the span-wise wavelength of stream-wise vortices in the shear later (λ_{zsl}) and in the wake (λ_{zk}) could be estimated as $\lambda_{zsl}/D \sim 0.1 \sim 25/\sqrt{\mathrm{Re}}$ and $\lambda_{zk}/D \sim 1$, respectively, at $\mathrm{Re} = O\left(10^4\right)$. Based on these relationships, the present mesh resolution $\Delta z/D \leq 0.018$ was considered to be sufficient to resolve the span-wise wavelengths of the stream-wise vortices in the wake and in the shear layers for Re = 50000.

3.4. On statistical convergence

The solution was started from the initial flow field at rest and approximately 290 time units have been simulated. The time-averaged solution, which corresponds to approximately 45 vortex shedding periods (N_{vs}), was computed during the last 100 time units. The time-averaging operator is denoted by $\langle\rangle$.

The special run was performed to check the sensitivity of results to statistical convergence. Due to resource limitations, the H2 grid was reduced to the span length of $4 \times D$ and the simulation was run with the total duration of approximately 580 time units. The prime flow features like the drag, lift coefficients, the recirculation zone length and the Strouhal number were time-averaged during 45, 90 and 135 vortex shedding periods. Table 1 summarizes these results.

It can be observed that all parameters were converged reasonably well with the dispersion of about 0.6%. Also, we calculated the Strouhal number based on the time signals of the lift coefficient, St_L, and the velocity, sampled at the downstream location ($x/D = 3$, $y/D = 0$), with the difference between them around 2%.

Table 1: Statistical convergence effects on the integral flow parameters

N_{vs}	$\langle C_d \rangle$	$-\langle C_l \rangle$	St_L	St_p	$\langle L_d \rangle$
45	0.502	1.076	0.375	0.386	0.782
90	0.499	1.088	0.374	0.379	0.787
135	0.497	1.087	0.372	0.379	0.792

3.4.1. Influence of the span length

The selection of span-wise lengths is always an important concern for numerical simulations [9], [11], [34]. Several preliminary runs were performed using the low-resolution mesh to investigate the span effects. For this purpose, besides the baseline span length, $L_z = 10 \times D$, the lengths, $L_z = 4 \times D$ and $L_z = 16 \times D$ were investigated. These additional meshes were designed in the similar way as H1 and maintained a modulation of the number of points to keep an equivalent grid spacing in the span-wise direction. The time-averaged solutions for all cases were sampled throughout the time of 45 vortex shedding periods.

Figure 4 displays some results obtained for $L_z = 4 \times D$, $L_z = 10 \times D$ and $L_z = 16 \times D$. We concentrated here on the mean drag, lift and pressure coefficients and the Strouhal number, since these parameters are available from the experiments [7], [8]. Summary of the results is provided in Table 2.

The pressure on the surface of the semi-circular cylinder was used to integrate the drag and lift coefficients, C_d and C_l. The mean drag and lift coefficients were converged to $\langle C_d \rangle = 0.512 \pm 1\%$ and $\langle C_l \rangle = -0.988 \pm 3\%$. The spectra from all three runs revealed the corresponding Strouhal number, $\mathrm{St} = f_{vs} D/U_\infty = 0.396$, where f_{vs} is a characteristic frequency of the vortex shedding.

The mean pressure coefficient is $\langle C_p \rangle = 2(\langle p \rangle - p_\infty)/(\rho_\infty U_\infty^2)$, where p_∞ is

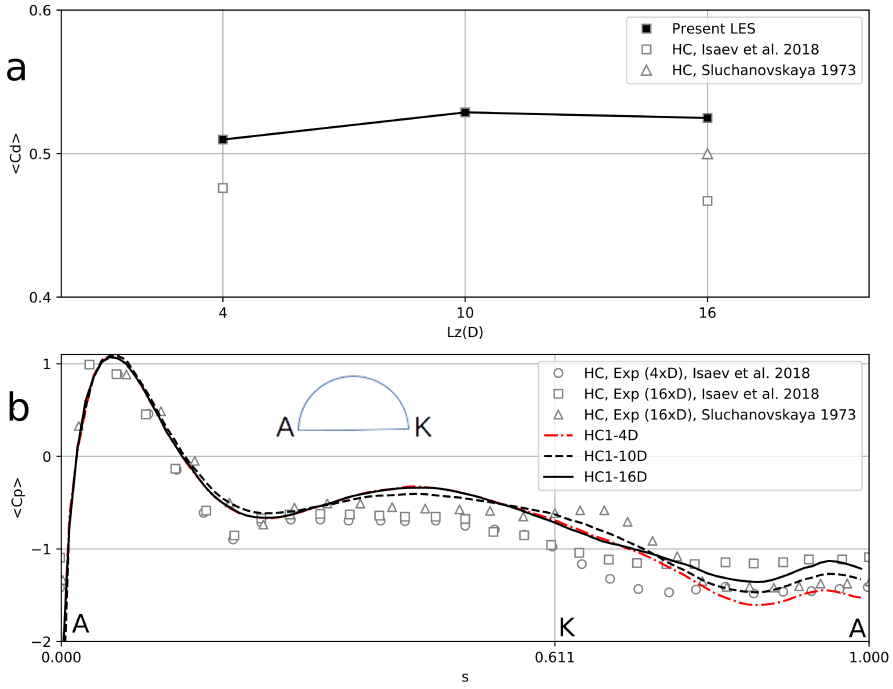

Figure 4: Mean drag (a) and pressure (b) coefficients as function of the span length ($L_z = 4 \times D, 10 \times D, 16 \times D$) for the flow over a semi-circular cylinder at Re = 50000

Table 2: Main flow parameters for the flow over the semi-circular cylinder at Re = 40000 − 50000: influence of the span length

Contributors	Method	L_z	$\langle C_d \rangle$	$-\langle C_l \rangle$	St_p
Sluchanovskaya [7]	EXP	$16 \times D$	0.5	1.1	
Isaev et al. [8]	EXP	$16 \times D$	0.467	0.634	0.41
Isaev et al. [8]	EXP	$4 \times D$	0.476	0.816	0.44
HC1-4D	LES-TKE	$4 \times D$	0.511	1.021	0.396
HC1-10D	LES-TKE	$10 \times D$	0.529	0.986	0.396
HC1-16D	LES-TKE	$16 \times D$	0.523	0.957	0.396

the free stream pressure. The distributions of $\langle C_p \rangle$ collapsed quite well. Some discrepancies between $L_z = 4 \times D$ and $L_z = 10 \times D - 16 \times D$ were observed at the suction side of the bluff-body. These deviations can be explained by stronger vortex shedding closer to the base of HC. The shortest L_z led to shortened length in the formation of the vortex and increased fluctuations in the streamwise velocity [9]. In addition, some differences in the flow dynamics inside of the recirculation bubble attached to the suction side of HC should be considered.

From the experimental point of view, the recent measurements by Isaev et el.[8] did not reveal significant $(5 - 10\%)$ variance of $\langle C_d \rangle$ due to the span length. However, approximately 7% difference was reported for the corresponding Strouhal numbers between $L_z = 4 \times D$ and $L_z = 16 \times D$. The tendency to decrease of the mean coefficient towards the highest span length was found as well. The measured mean lift coefficient differed by about 20% between these two span-to-diameter ratios. However, a critical remark could be provided here. The baseline span length of the experiment was set to $L_z = 16\ D$. However, the pressure measurements was conducted only in one central section and the span averaging was not provided. Additionally, Isaev et al.[8] studied the variant of two 0.13 m side discs installed symmetrically to the left and right of the central measuring section with the distance between the side discs equal to $4 \times D$. In practice, this setup varied from the assumed infinitely extending lateral walls, which were assumed in the present (and other) studies. These findings possibly

can explain observed deviations between numerical and experimental results, as well as about 7% and 40% inconsistency between experimental data by Isaev et al. [8] and measurements by Sluchanovskaya [7] for $\langle C_d \rangle$ and $\langle C_l \rangle$, respectively.

Since the examined flow past the semi-circular cylinder is a superposition of the flow over the circular and square cylinders, it is interesting to analyze available and relevant data for these two problems.

With respect to the circular cylinder, the present findings were consistent with the recent results by Garcia et al. [34]. They numerically investigated the span effects for the flow over a circular cylinder at Re = 10000 for the different span lengths in the range from $L_z = 0 - 10 \times D$. Garcia et al. [34] summarized that the turbulence statistics in the wake were very similar for $L_z = \pi \times D$ and $L_z = 10 \times D$. No variation for the Strouhal number was observed, and all cases were converged to St = 0.2. Effects of L_z on turbulence kinetic energy to lift force dependency was very small for $L_z \geq \pi \times D$, meaning that three-dimensional turbulence fully dominated.

It is interesting that Cao and Tamura [9] numerically investigated the span effects for the flow over a circular cylinder at Re = 130000. Their LES study showed the tendency of $\langle C_d \rangle$ and fluctuating lift, $\langle C_l' \rangle$, to increase against reduced L_z, which was consistent with the experimental study obtained by Szepesssy and Bearman [35]. However, they concluded that $L_z = 9 \times D$ was reasonably sufficient to investigate three-dimensional effects, and the numerical results obtained using $L_z = 9 \times D$ were approximately consistent with experimental measurements with sufficiently long span-wise lengths.

Lately, Cao and Tamura [11] presented LES results of the flow over a square prism at Re = 22000. They investigated this case for $L_z = 4 \times D$ and $L_z = 14 \times D$ and found that the span- and time- averaged sectional drag coefficient was very close to that of the total drag coefficient, when $L_z = 4 \times D$. This confirmed the observation that, in general, the vortex strength shedding from the square cylinder on the cross sections does not change significantly when the span-wise length is extended to $14 \times D$, which can be explained by the fact that the square cylinder has the fixed separation points.

Finally, it could be considered that the span-wise length, $L_z = 10 \times D$, is reasonably sufficient for the present analysis to investigate the aerodynamic characteristics of the flow past HC.

4. Results

4.1. Overview

Simulated cases are listed in Table 3, with mesh according to Sec. 3.3. Turbulence model is either the k-equation eddy-viscosity SGS model (TKE) or the dynamic k-equation eddy-viscosity SGS model (dTKE).

Table 3: Run matrix: Mesh, turbulence model, Mach and Reynolds numbers

Run	MS	TM	M	Re
HC1-TKE	H1	TKE	0.03	50000
HC2-TKE	H2	TKE	0.03	50000
HC2-dTKE	H2	dTKE	0.03	50000

4.2. Mean flow features

The root-mean-square values of the aerodynamic coefficient were $C_d^{'} - \langle C_d \rangle = 0.381, 0.331, 0.332$ and $C_l^{'} - \langle C_l \rangle = 1.22, 1.21, 1.22$ for the HC1-TKE, HC2-TKE, HC2-dTKE runs, respectively, which indicates that results were well converged [24].

Table 4 summarizes the main integral flow parameters as the lift C_l, drag C_d, pressure base C_{pb} coefficients and the Strouhal number St_p. Additionally, the mean length of the detached recirculation zone L_d was added for quantitative comparison and analysis of results.

The distribution of the mean pressure coefficient, $\langle C_p \rangle$, and normalized vorticity, $\langle \Omega \rangle / \sqrt{\mathrm{Re}}$, over the semi-circular cylinder are plotted in Figure 5. The numerical results satisfactorily replicated experimental data by Sluchanovskaya [7]. The present numerical results obtained with the low and high resolution grids fully collapsed. There were some small deviations of $\langle C_p \rangle$ and $\langle \Omega \rangle$ at the

Table 4: Integral flow parameters obtained from the experimental and numerical results for the flow past the semi-circular cylinder at $\mathrm{Re} = 40000 - 50000$

Contributors	Method	L_z	$\langle C_d \rangle$	$-\langle C_l \rangle$	$-\langle C_{pb} \rangle$	St_p	$\langle L_d \rangle$
Sluchanovskaya [7]	EXP	$16 \times D$	0.5	1.1	0.62		
Yamagata et al. [36]	EXP	$12.7 \times D$	0.37	0.54		0.37	
Isaev et al. [8]	EXP	$16 \times D$	0.467	0.634	0.96	0.41	
Isaev et al. [8]	EXP	$4 \times D$	0.476	0.816	0.98	0.44	
Isaev et al. [8], [13]	URANS-SST	$0 \times D$	0.459-0.55	0.66-1.177	0.65-0.73	0.393-0.472	
HC1-TKE (11M)	LES-TKE	$10 \times D$	0.529	0.986	0.62	0.396	0.86
HC2-TKE (25M)	LES-TKE	$10 \times D$	0.468	1.055	0.54	0.371	0.86
HC2-TKE (25M)	LES-dTKE	$10 \times D$	0.469	1.035	0.54	0.372	0.78

suction side of HC, which can be explained by the slightly different flow patterns revealed by the LES runs.

Figure 6 compares time-averaged flow patterns calculated by the present LES runs. One can see that the topology of the flow was quite similar for all cases. Thus, the prime detached recirculation bubble at the backward side of HC contained two cores and one small counter-rotating vortex. The recirculation zone attached to the suction size of HC consisted of the prime core and two small counter-rotating vortices. Small deviations between three runs could be observed, but, in general, the flow patterns were quite similar to each other.

The present $\langle C_p \rangle$ satisfactorily matched the measurements by Sluchanovskaya [7]. It will not be superfluous to take into consideration that reasonable match was achieved for the mean normalized vorticity, $\langle \Omega \rangle$, with experimental results by Son and Hanratty [14], obtained for the circular cylinder at $\mathrm{Re} = 20000$ and $\mathrm{Re} = 50000$.

One can see that the stagnation point ($s = 0$) for HC was moved up along the pressure side approximately to $s = 0.06$ (Fig. 5). The peak values of $\langle C_p \rangle$ and the deep descent of Ω were vanishing mostly to zero at this point. The location of the stagnation point can be related to the flow separation angle, θ at the pressure side of HC. Here, θ was defined as angular coordinate starting from the leading edge. All $\langle \Omega \rangle$ curves presented in Figure 5 collapsed well up to $\theta \approx 90^\circ$. As known from measurements [14], the separation for CC for these particular Reynolds number should take place at $\theta = 78^\circ$, which was consistent

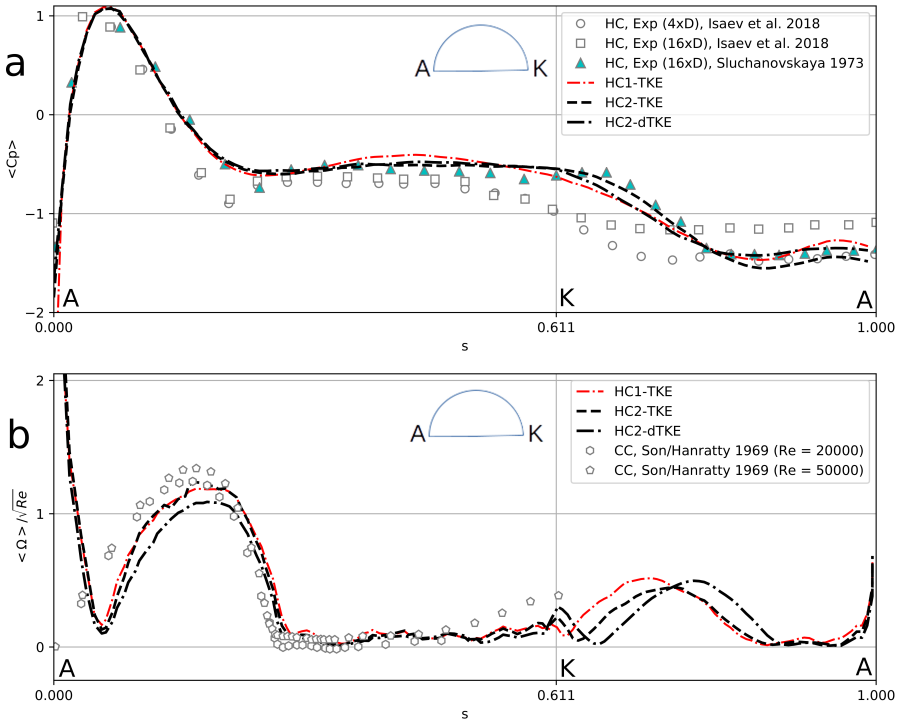

Figure 5: Profiles of the mean pressure coefficient (a) and normalized vorticity (b) along the circumferential coordinate, s (see Fig. 3), for the flow over a semi-circular cylinder at $\mathrm{Re} = 50000$

with the analytical solution from the boundary layer theory. It is interesting that the present predictions were consistent with authors' previous LES results for CC [4], where $\theta \approx 86^\circ - 88^\circ$ were obtained.

The value of $\langle C_{pb} \rangle$ on the cylinder's surface at the trailing edge can be defined as the base suction coefficient $\langle C_{pb} \rangle$. The calculated values $-\langle C_{pb} \rangle = 0.54 - 0.62$ correlated well with the experimental value by Sluchanovskaya [7], $-\langle C_{pb} \rangle = 0.62$. It is interesting to note, that Isaev et al. [8] reported significantly differing (by 36%) values of the mean base suction coefficient, $-\langle C_{pb} \rangle = 0.96 - 0.97$.

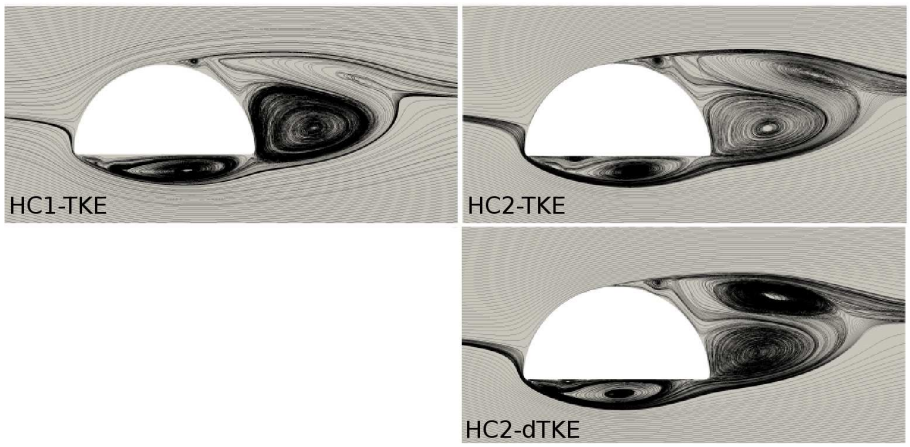

Figure 6: Time-averaged streamlines for the flow over a semi-circular cylinder at Re = 50000 computed in the $x - y$ plane at the middle of the span length

The mean drag coefficient was calculated to $\langle C_d \rangle = 0.463 - 0.512$, which was in reasonable agreement with experimental data by Sluchanovskaya [7] and Isaev et al. [8] of $\langle C_d \rangle = 0.467 - 0.5$. The mean, negative lift coefficient obtained by the present LES results was $-\langle C_l \rangle = 0.986 - 1.055$. These values were in good agreement with the experimental data of Sluchanovskaya [7], who measured $\langle C_l \rangle = -1.1$, and significantly over-predicted the measured data by Isaev et al. [8] of $-\langle C_l \rangle = 0.634 - 0.816$. Similar to a circular cylinder, the recirculation length of the detached recirculation bubble was defined as a distance between the base of the cylinder and the sign change of mean stream-wise velocity along the axial direction at $y/D = 0.25$. The computed recirculation lengths of the

detached separated zones were $\langle L_d \rangle = 0.78 - 0.86$.

Some discrepancies between the present LES and available measurements could be explained by the influence of chamfered corners of HC. The present simulations were performed for HC with the rounded corners of $r/D = 0.025$, while HC with sharped edges was used in experiments. The influence of edge rounding was investigated by Carassale et al. [37], who confirmed experimentally the positive effects like reducing the drag force and the fluctuations of the lift due to the vortex shedding. Carassale et al. reported that the drag coefficient decreased about by $\approx 15\%$ and the fluctuations of the lift coefficient reduced by $\approx 20\%$ for the square cylinder with the rounded corners, $r/D = 1/15$. However, it should be taken into account that the present results were computed for HC with the rounded radius, $r/D = 0.025$, approximately 3 times lower than what Carassale et al. [37] used. Nevertheless, the aforementioned effects like reducing of the drag and root-mean-square values of the lift should be considered to compare the present results with experiments by Sluchanovskaya [7] and Isaev et al. [8].

4.3. First and second order statistics

Figure 7,a shows the profiles of the mean stream-wise velocity $\langle U \rangle / U_\infty$ along the centerline. Here, available experimental and numerical results for the circular ([15], [17], [4]) and square ([20],[21], [22], [23], [24]) cylinders were added to assess the present results qualitatively. A critical remark should be provided here. First, most of the discussed results have been restricted to the Reynolds numbers, $\mathrm{Re} = 22000 - 50000$. Second, the experimental data by Sanquer et al. [22] were measured for the rectangular cylinder of the $2:1$ ratio and the obstacle Reynolds number, $\mathrm{Re} = 5684$ and, therefore, does not fit the general trends.

The minimum values of the mean stream-wise velocity, $\langle U \rangle / U_\infty$, predicted in the present simulations were from -0.18 to -0.2. This was close to the data, obtained by LES of CC [4] and experimental data by Durao et al. [20], McKillop and Durst [15], Lyn et al. [21] and Trias et al. [24] for SC. Overall, the calculated

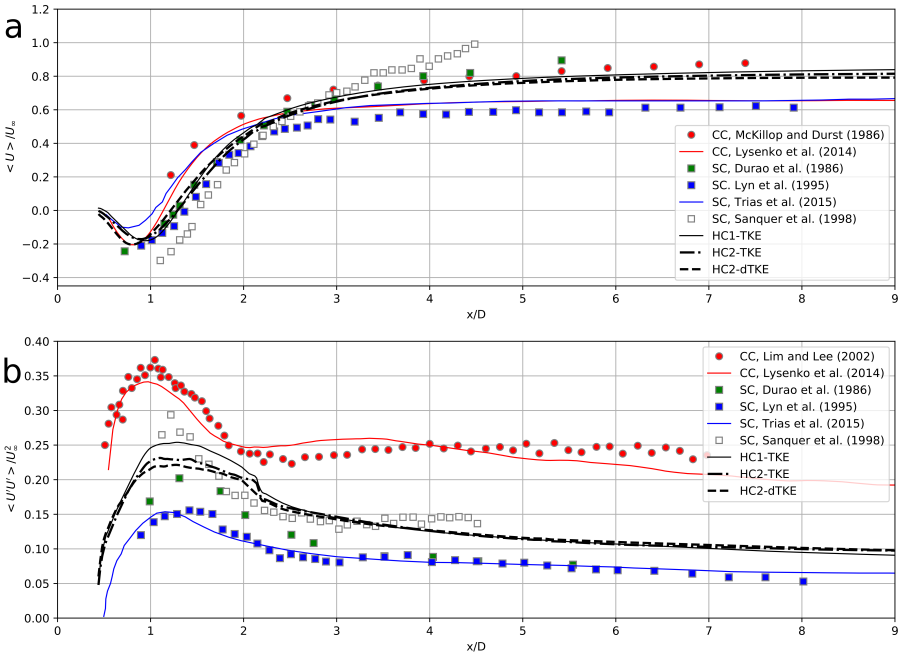

Figure 7: Profiles of the mean stream-wise velocity, $\langle U \rangle / U_\infty$ (a), and normal stresses, $\langle U'U' \rangle / U_\infty^2$ (b), in the wake centerline for the flow over a semi-circular cylinder at Re = 50000

curves collapsed well and replicated the same experimental trends obtained by Durao et al. [20] and McKillop and Durst [15]. Also, it is interesting to note that the LES by Lysenko et al. [4] obtained for CC agreed well with DNS by Trias et al. [24] for SC.

Figure 7,b shows the profiles of the mean normal stress, $\langle U'U' \rangle / U_\infty^2$, along the centerline. It is interesting to note the large gap between the mean normal stresses, measured and calculated for CC and SC. The peak values of the normal stresses, which corresponded to the prime separation bubble, differed more than twice between CC and SC data. The present LES curves collapsed quite well and qualitatively trended to the data for CC and SC. There were small discrepancies between the calculated data obtained at the low and high-resolution meshes inside the recirculation zone. Overall, the present LES results for HC were close to data by Durao et al. [20] and Sanquer et al. [22] for SC.

Figure 8 shows the time-averaged stream-wise velocity and normal stress in the near wall region of the suction side of HC. Both $\langle U \rangle / U_\infty$ and $\langle U'U' \rangle / U_\infty^2$ predicted by the present LES were qualitatively similar to the experimental data by Minguez et al. [23] and Lyn et al. [21], as well as the DNS data by Trias et al. [24], obtained for the flow over square cylinder at Re = 22000. It is worth noting that in the present case the thickness of the attached recirculation zone in these locations were 15% less compared to the SC case.

4.4. One-dimensional energy spectra and shear-layer instability

Figure 9 illustrates the formation of the vortex street and coherent flow structures downstream of the semi-circular cylinder, showing the Q-criterion, $Q = S^2 - \Omega^2 = 10^4$, where S is the strain rate and Ω is the vorticity. The visualization displays the capability of the present simulations to resolve wide range of vortex structures that developed in the turbulent wake. The vortex cores, which are originated during separation of the laminar boundary layers from the pressure and suction side of the cylinder surfaces, were identified clearly. After formation the vortex cores convected further downstream by the mean flow.

The vortex shedding instability had a characteristic frequency of $f_{vs} =$

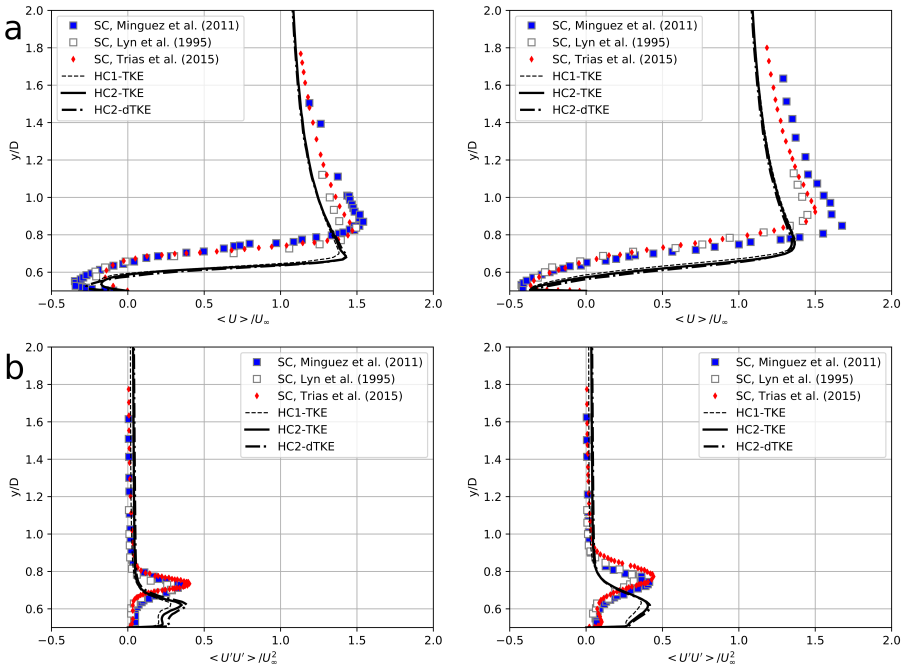

Figure 8: Profiles of the mean stream-wise velocity, $\langle U \rangle / U_\infty$ (a), and normal stresses, $\langle U'U' \rangle / U_\infty^2$ (b) at two different locations: $x/D = -0.125$ (left) and $x/D = 0.125$ (right) for the flow over a semi-circular cylinder at $\mathrm{Re} = 50000$

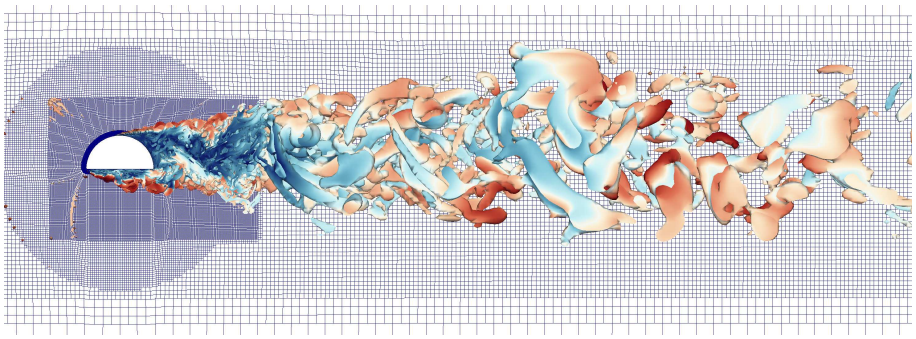

Figure 9: Visualization of flow structures (HC2-dTKE run) obtained for the flow past a semi-circular cylinder. Iso-surfaces of the Q-criterion ($Q = S^2 - \Omega^2 = 10^4$, where S is the strain rate and Ω is the vorticity)

$\mathrm{St}_p U_\infty/D$, where St_p is the Strouhal number in the post-shear-layer transition. To compute both characteristic frequencies of the vortex shedding and KH instability, the velocity signal was sampled in the six velocity probes located at the vicinity of the bluff-body (Figure 10,a). The probes were located inside the detached separated zone (labeled RZ1 and RZ2), as well as in the attached recirculation zone (RZ3), and in the locations where the shear layer instabilities develop from both pressure and suction sides of the cylinder (KH1 and KH2). The prime probe was located at the central x-axis at $x/D = 3$ (marked P). The spectra calculated from these time series were then averaged in the span-wise direction (13 probe locations uniformly distributed were used) to increase the statistical sample. To obtain the one-dimensional spectra, both Fast Fourier transform (FFT) and the Welch periodogram technique [38] were used. Table 5 summarizes the results of calculations.

The computed values of the Strouhal number of the vortex shedding frequency at the prime probe (P) were $\mathrm{St}_p = 0.372 - 0.396$, which matched well the experimental data by Yamagata et al. [36] ($\mathrm{St}_p = 0.37$), whereas significantly under-estimating the experimental data by Isaev et al. [8], who predicted $\mathrm{St}_p = 0.41$ and $\mathrm{St}_p = 0.44$ for $L_z = 4 \times D$ and $L_z = 16 \times D$, respectively. One of possible explanations may be the fact that experimental values by Isaev et al. [8] were obtained from the signals of the pressure coefficient. In practice, it was somewhat unusual, since most of the reported experimental St have been extracted from the time series of the lift coefficient or velocity signals. Another possible explanation was discussed in Sec. 4.2 and could be related to the chamfered edges of HC. In this case some reduction of St could be expected as well since the Strouhal number is closely related to the lift force, which have been confirmed by measurements of Carassale et al. [37].

The Strouhal numbers obtained from the probes located within the detached recirculation zone had approximately the same values as the prime Strouhal number. It is interesting that the recirculation zone attached to the suction side of the obstacle had significantly higher pronounced frequency and was characterized by $\mathrm{St} = 1.691 - 1.72$. Figure 10,b-d presents normalized Welch spectra for

the attached and detached recirculation regions for HC2-TKE and HC2-dTKE.

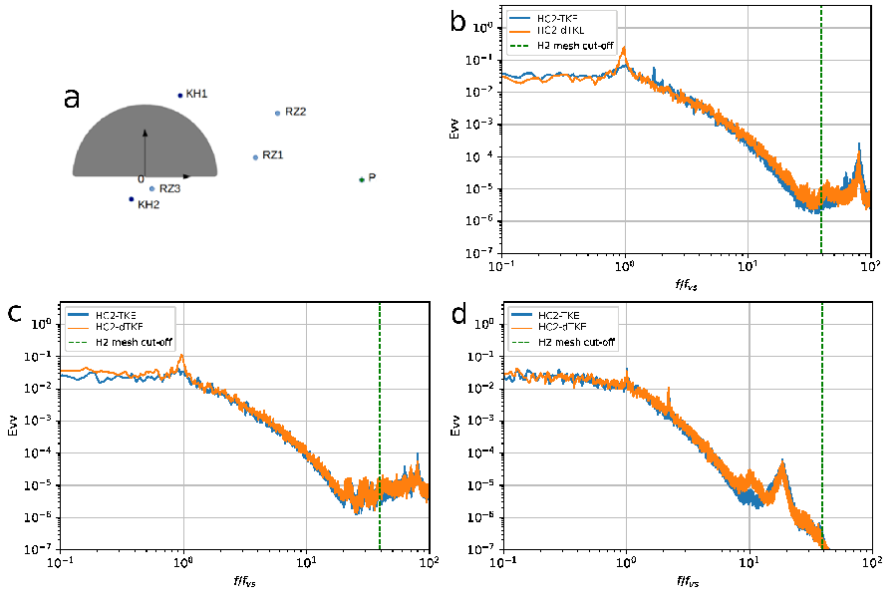

Figure 10: A general scheme of the probe locations for data sampling (a). One-dimensional spectra of the transverse velocity in the vicinity of the semi-circular cylinder at the detached (b,c) and attached (d) recirculation zones.

Table 5: Near wake dynamics

Run	St	St_{RZ1}	St_{RZ2}	St_{RZ3}	f_{vs}/f_{kh1}	f_{vs}/f_{kh2}
HC1-TKE	0.396					
HC2-TKE	0.371	0.371	0.371	1.691	10.71	10.68
HC2-dTKE	0.372	0.372	0.372	1.72	9.94	9.97

One-dimensional frequency spectra are displayed in Figure 11. The spectra were extracted from the sampling signals at the downstream location $x/D = 3$, $y/D = 0$. The frequency was nondimensionalized by the Strouhal shedding frequency (f_{vs}). The experimental results of Ong and Wallace [16], Sanquer et al. [22], Parnaudeau et al. [18] and a $-5/3$ slope are shown as well. The present numerical data sets yielded very similar power spectra. The HC1-TKE run pro-

vided a slightly dissipative spectrum, which was obtained using the lower resolution grid H1. The LUST convective scheme provided the not over-dissipative sub-grid modeling by reproducing the inertial subrange clearly for a large spectral range. Also, the same trends as the measured spectra by Ong and Wallace [16] (CC), Sanquer et al. [22] (SC) and Parnaudeau et al. [18] (CC) were reproduced.

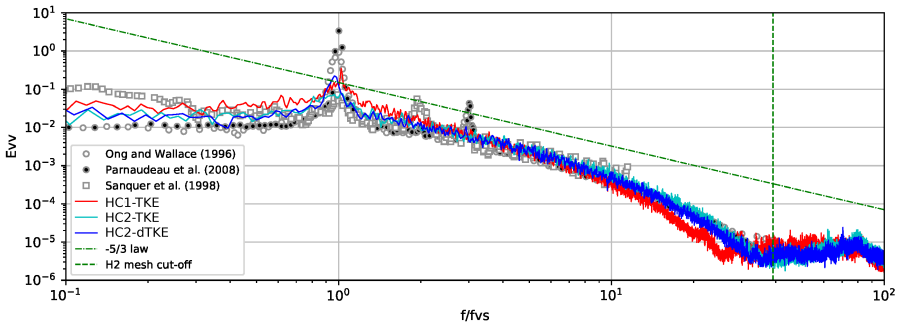

Figure 11: One-dimensional spectra of the transverse velocity in the wake for the flow over the semi-circular cylinder at Re = 50000

From the experimental point of view, several studies investigating the separated shear-layer in the near wake of CC are available in the literature [39], [40], [41], [42], [43], [44], [45]. Bloor [39] seems to be the first who studied the frequency of the shear layer instability waves. She demonstrated that the shear layer instability frequency scaled approximately with $\sqrt{\mathrm{Re}}$, by considering the thickness and velocity of the separating laminar boundary layer. Lately, Prasad and Williamson [44] provided re-evaluation of all data and reported that the exponent p in the expression $f_{kh}/f_{vs} = A \times \mathrm{Re}^{p} = 0.0235 \times \mathrm{Re}^{0.67}$ was significantly greater than 0.5 in every case.

Lander et al. [46] investigated the mechanisms of transition in the shear layers of a square cylinder at Reynolds number range $15000 < \mathrm{Re} < 75000$. They derived the relation $f_{kh}/f_{vs} = 0.18 \times \mathrm{Re}^{0.6}$, which was based on the hot-wire measurements, PIV and DNS studies. The numerical data of Brun et al. [47] and Trias et al. [24] were analyzed as well. These data were at Re = 20000

(LES), Re = 22000 (DNS) and Re = 27000 (laser Doppler velocimetry, LDV).

Recently, Moore et al. [48] carried out a detailed experimental study of the separated shear layers stemming from rectangular sections with aspect ratios of $5:1$, $3:1$ and $1:1$ in the range $13400 < \mathrm{Re} < 118000$ (here, the Reynolds number was based on the body thickness). It was interesting that experimental results for f_{kh}/f_{vs}, obtained by Moore et al. [48] for the $5:1$ rectangular section, were somewhere between the square prism and circular cylinder. Some limited compiled data are plotted in Figure 12. Moore et al. [48] reported that all geometries fitted well with a power law. However, both the exponent and the coefficient were different for each bluff-body geometry.

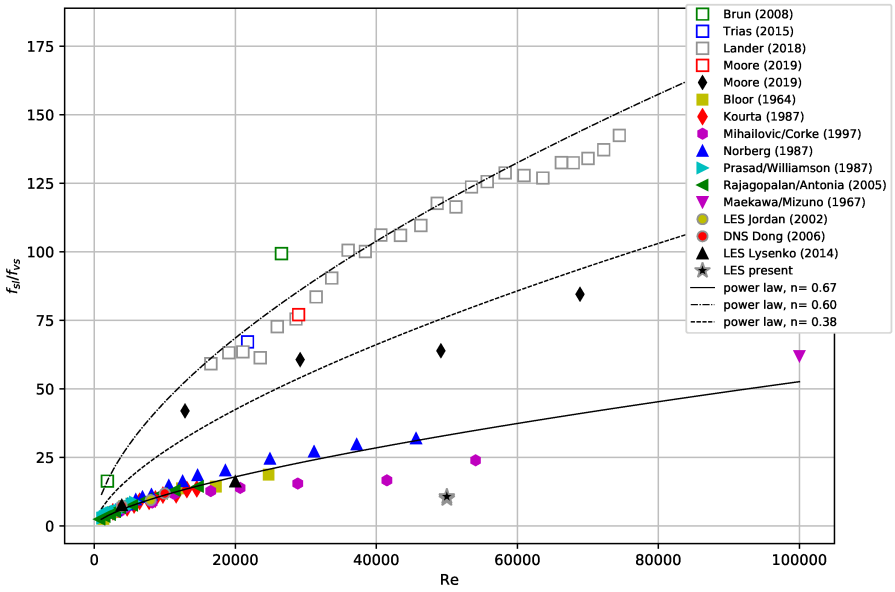

Figure 12: Variation of normalized shear layer frequency with Reynolds number: experimental and computational results

On a dimensional basis, one can expect that the shear layer frequency will scale with a characteristic velocity and length scale in the form of U_{sep}/θ_{sep}, where U_{sep} is the velocity outside the boundary layer at the separation point, and θ_{sep} is the momentum thickness of the separated shear layer. Bloor [39] suggested that the momentum thickness scales with the boundary layer thickness

just before separation, which itself scales as $\mathrm{Re}^{-0.5}$. In terms of the Strouhal number and base suction coefficient (C_{pb}), the following expression can be written [49] as $f_{kh}/f_{vs} \approx \mathrm{Re}^{0.5}\,(U/U_{sep})\,(1/\mathrm{St}) \approx \mathrm{Re}^{0.5}\,(1-C_{pb})^{0.5}\,(1/\mathrm{St})$. If it can be assumed that over a large range of Re, C_{pb} is approximately constant, then one finds the expression used by Bloor: $f_{kh}/f_{vs} \approx \mathrm{Re}^{0.5}$.

In practice, the characteristic lengths and velocities are somewhat different from the values assumed above. In particular for the circular cylinder, it was found that there is indeed a variation of base pressure C_{pb} over a range of Re, and also that the movement of the transition point upstream as Re increases affects the shear layer frequency [49]. Moore et al. [48] suggested to explain these variations by considering the dynamics at separation for each body, where the shedding frequency of the KH events near separation ought to scale inversely with the thickness of the separating boundary layer.

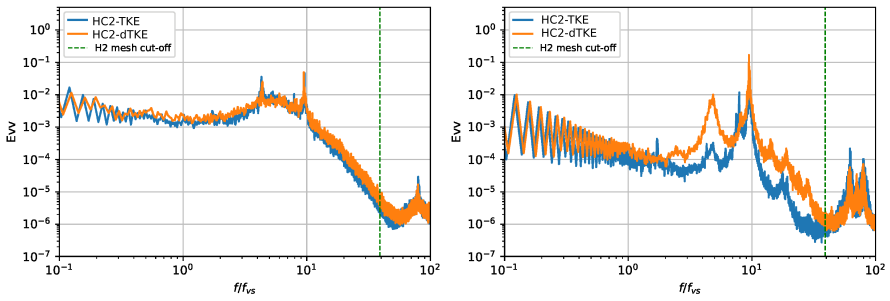

Figure 13: One-dimensional spectra of the transverse velocity in the shear layers from the pressure (KH1) and suction (KH2) sides of the semi-circular cylinder at Re = 50000

The authors' previous LES results calculated for the circular cylinder flow revealed $f_{kh}/f_{vs} = 7.6$ and $f_{kh}/f_{vs} = 16.2$ for Re = 3900 [3] and Re = 20000 [4], respectively. These results were in good agreement with the available experimental data. In addition, the DNS study by Trias et al. [24] provided for the square prism at Re = 22000 a relatively broadband frequency peak at $f_{kh}/f_{vs} \sim 60$. Cao and Tamura [9] calculated the peaks of shear-layer frequencies as $f_{kh}/f_{vs} = 15-17$, which were much smaller than the LDV measurement

by Minguez et al. [23] ($f_{kh}/f_{vs} \approx 45$).

The present LES results obtained for the semi-circular cylinder predicted $f_{kh}/f_{vs} = 9.94 - 10.71$. Figure 13 presents the Welch spectra computed for HC2-TKE and HC2-dTKE. These results were close to the experimental trend, obtained for CC. Also, it will not be superfluous to consider that shear layers frequencies calculated from the pressure and suction sides of HC had approximately similar values. However, the lack of the qualitative and quantitative experimental data for HC did not allow to make more specific conclusions.

5. Discussion

In this section, the differences and similarities between CC, SC and HC, as well as major sources of errors in numerical simulations and physical measurements are discussed.

5.1. Comparison of integral flow parameters for the semi-circular, circular and square cylinders

Analogy of the aerodynamics parameters of the circular, semi-circular and square cylinders (CC, HC and SC, respectively) at Re $= 20000 - 50000$ is of interest. Here, we limited comparison to the three prime integral parameters: $\langle C_d \rangle$, $\langle C_l \rangle$ and St_p. From the numerical point of view, only LES studies were considered. The collected data for SC were extracted from the studies by Cao et al. [25]. The DNS results by Trias et al. [24] were used as reference data as well. Data related to CC were taken from the works by Lysenko et al. [4] and the recent study by Plata et al. [19]. Main results for HC were represented by the present LES and measurements by Sluchanovskaya [7] and Isaev et al. [8]. All data are summarized in Table 6.

The mean drag coefficient for SC was predicted as $\langle C_d \rangle = 2.02 - 2.77$, which was approximately twice the value of its circular analogue $\langle C_d \rangle = 0.98 - 1.39$. The mean drag coefficient for HC in its turn was anticipated approximately half of that for CC, $\langle C_d \rangle = 0.467 - 0.529$. The mean lift coefficient was expected to

Table 6: Overview of the experimental and numerical works (LES) for the different bluff-bodies (BB) flows at $\mathrm{Re} = 20000 - 50000$

BB	Exp/Num	$\langle C_d \rangle$	$-\langle C_l \rangle$	St_p	References
CC	EXP	1.1-1.2		0.187-0.19	Lysenko et al. [4], (Table 2); Plata et al. [19], (Table 4)
CC	NUM	0.98-1.39		0.17 - 0.2	Lysenko et al. [4], (Table 2); Plata et al. [19], (Table 4)
HC	EXP	0.467-0.5	0.634-1.1	0.41-0.44	Sluchanovskaya [7], Isaev et al. [8]
HC	NUM	0.469-0.529	0.958-1.055	0.37-0.396	Present LES
SC	EXP	2.05-2.34		0.122-0.14	Cao et al. [25] (Table 1)
SC	NUM	2.02-2.77		0.09-0.15	Cao et al. [25] (Table 1)

be zero for SC and CC due to the symmetry, meanwhile $-\langle C_l \rangle = 0.634 - 1.1$ was predicted for HC, which was the fundamental difference between these bluff-bodies.

The computed and measured Strouhal numbers for SC were in the range $\mathrm{St}_p = 0.1 - 0.15$. The results shown were roughly twofold from those that characterized the flow around a circular cylinder in the sub-critical regime, $\mathrm{St} = 0.17 - 0.20$. Furthermore, it is notable that the Strouhal numbers obtained for HC, $\mathrm{St}_p = 0.37 - 0.44$ were twice as large as for CC (assuming the minor difference in the vortex shedding for $\mathrm{Re} = 20000$ and $\mathrm{Re} = 50000$).

Figure 14 presents distributions of the mean pressure coefficient for CC, HC and SC obtained both numerically and experimentally. As already was discussed, the stagnation point of the incoming flow onto HC was located on the pressure side of the body, slightly above the leading edge. The pressure at this point was close to the dynamic pressure, $C_p \approx 1$. One of the interesting observations coming from Fig. 14 was related to the level of rarefaction of the separated zone detached from the backward side of bluff-bodies. On one hand, the highest level of rarefaction was found for SC, which was approximately half of its CC analogue. On the other hand, the level of rarefaction of CC was about half of HC. In addition, it is wise to mention that the pressure coefficient at the leading and trailing edges of HS was about the same despite the asymmetrical form of HC.

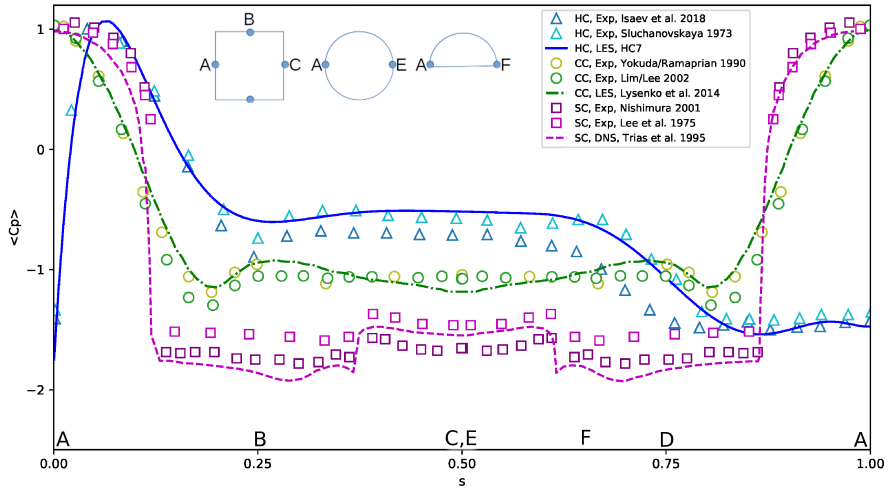

Figure 14: Mean pressure coefficient distributions for the flow over HC, CC and SC at Re = 20000 − 50000: Numerical and experimental results

5.2. Comparison with URANS results

From the numerical modeling point of view, it is interesting to compare the present LES results to calculations reported by Isaev et al. [8], [13], who have used the classical URANS approach and the family of the $k-\omega$ SST turbulence models for the flow over a semi-circular cylinder at Re = 50000, M = 0 − 0.5 and zero angle of attack. It is worth noting that Isaev et al. compared different computational codes and provided a systematic study on influence of the grid and numerical schemes factors for this test problem. Here, we only highlight some brief aspects. The main integral flow parameters are compared in Table 4.

It should be noted that the range of $\langle C_d \rangle$ obtained by URANS, $\langle C_d \rangle = 0.459 - 0.55$, and present LES, $\langle C_d \rangle = 0.469 - 0.529$, overlapped reasonably. Small discrepancies may be caused by different effects related to variation of the rounding radii. Thus, Isaev et al. [8], [13] used the grids with $r/D = 0.002 - 0.005$, while the present LES study was performed with $r/D = 0.025$. Apart from this, significant deviations for the lift coefficient and the Strouhal number were found. For the lift coefficient the present LES converged to $-\langle C_l \rangle \approx 1$,

while URANS calculations provided quite large variation from $-\langle C_l \rangle = 0.634$ to $-\langle C_l \rangle = 1.177$. The Strouhal numbers predicted by LES were $\mathrm{St} = 0.371-0.396$, which not even overlapped the URANS data, $\mathrm{St} = 0.393 - 0.472$.

Such large variations could be explained by the three-dimensional (span-wise length) effects. The difference in modeling of the turbulence should be considered as well. Figure 15 compares the flow patterns obtained by the present LES and URANS. The similarities between calculations are evident, however, some noticeable differences could be discussed. Using the definition of the recirculation zone length, provided in Sec. 3.1, one can see clearly that LES provided L_r twice as wide compared to the URANS data. The formation of the separated recirculation zone attached to the backward side of HC originated by the separation and convection of the vortices in the shear layers from the pressure and suction sides. In practice, the prime vortex shedding frequency is a superposition of these two processes. The shortest recirculation length provided higher shedding frequency and Strouhal number. Therefore, the URANS calculations provided the largest Strouhal numbers. A second difference was the existence of small counter-rotating vortices revealed by the present LES, which were located inside the detached and attached reversed bubbles. The different characteristic frequencies of these detached and attached recirculation zones was another interesting finding of the present study. It is worth noting that Isaev et al. [8], [13] reported a bi-modal distribution of the drag force as well, which could support the present findings.

The differences between the lift coefficients, predicted by URANS and LES, could be explained by dissimilarity in the flow patterns as well. In addition, three-dimensional effects should be considered.

5.3. Influence of numerical and experimental errors

In practice, disagreements between experimental data and numerical results can be determined by errors in numerical simulations and in experiments. The computational errors can be divided into discretization and modeling sub-sets.

From the numerical point of view, many factors can affect the quality of the

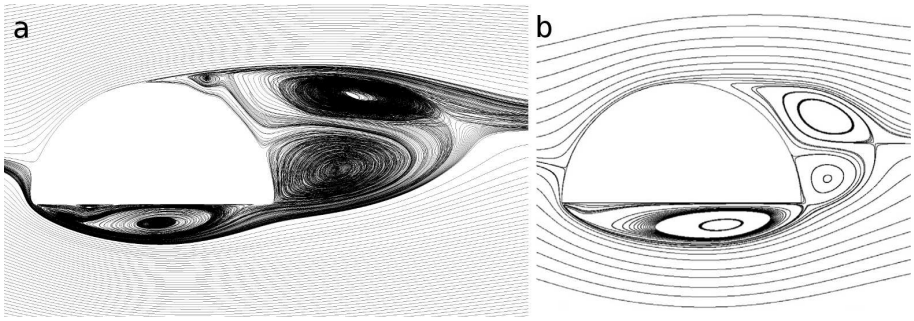

Figure 15: Comparison of the time-averaged patterns of the flow over the semi-circular cylinder at Re = 50000 obtained by the present LES, HC2-dTKE (a) and URANS (b), [8]

LES. Among them are the size of computational domain, the grid resolution, the sub-grid scale model, the boundary conditions, the numerical schemes and the computational code. The collected numerical results for CC, SC and HC revealed a great dispersion for all bulk parameters like the mean drag and lift coefficients and their root-mean-square values, the Strouhal number and the recirculation zone length. In particular, for SC, Trias et al. [24] concluded that this flow formed a major challenge to LES techniques without finding a definite solution. Based on the large dispersion found for CC and HC, it is possible to extend this conclusion for the circular and semi-circular cylinders as well (Table 6).

It is worth noting that the physical experiments can contribute a large source of errors as well. This finding was supported by the assembled experimental data for CC, SC and HC, where a large dispersion of the bulk quantities was observed as well (Table 6). Trias et al. [24] reported that the accurate prediction of the drag force is not trivial [50]. The main factors like the free-stream turbulence intensity and the blockage effects need to be considered. In particular, the free-stream turbulence intensity tends to reduce drag. The blockage effects may be relatively low, but certainly affect the measured drag coefficient (and other related parameters).

For this particular case, two sets of experimental data were used. It was observed, for example, that the measured values of the lift coefficient varied

as $-\langle C_l \rangle = 0.65 - 1.1$. Moreover, the recent experiment [8] revealed a strong dependency on the measured results from the span length. Furthermore, it must be considered, that the pressure coefficient was measured only in a $x - y$ plane and three-dimensional effects (span variation) were not captured. Finally, it must be noted that the experimental Strouhal number was calculated by the spectral analysis of the pressure signal, which was sampled at the leeward side of the bluff-body, as opposed to many experimental works, where St_p is calculated either from the time series of the lift coefficient or from the transverse component of velocity in the wake.

6. Concluding remarks

The flow past a semi-circular cylinder at zero angle of attack, $\mathrm{Re} = 50000$ was computed using the LES technique as the consistent continuation of the previous LES studies for the circular [3], [4] and triangular [5] cylinders. The fully conservative, second-order finite-volume method has been used together with the k-equation SGS model, implemented in OpenFOAM.

The present results were compared against experimental data available for the circular, square and semi-circular cylinders. Available LES and DNS results for the flow over circular and square cylinders at the similar Reynolds numbers were used to assess the quality of the present results. Apart of this, some discussion and comparison with the recent URANS data were provided. The present simulations showed that this test case involved remarkably complex flow features as a superposition of the square and circular cylinder flows. Similarity and dissimilarity between these bluff-bodies were presented based on the bulk parameters and local distributions of the time-averaged pressure coefficient and velocity field.

The collected numerical and experimental results obtained for the circular, semi-circular and square cylinder flows at $\mathrm{Re} = 20000 - 50000$ revealed a significant dispersion for the prime flow parameters, which will continue to be a major challenge to the large-eddy simulation in future [24], especially for the highest

Reynolds numbers, Re $> 10^5$. Moreover, the negative lift coefficient may be one of the additional challenges for both numerical simulations and experimental measurements.

Finally, the reasonable overlapping and consistency with available experimental and numerical data was found, which may suggest the adequacy and the accuracy of the present results to predict the turbulent separated flow past the semi-circular cylinder using the large-eddy simulation technique. It is worth noting that the relative uncertainty should be taken into consideration since only solid validation was available only for the distribution of C_p along the cylinder, C_d and C_l coefficients and the Strouhal number, which are available in the literature.

Acknowledgements

We are grateful to the Norwegian Meta center for Computational Science (NOTUR) for providing the uninterrupted HPC computational resources and useful technical support. (project No. NN9400K).

Compliance with ethical standards

- Funding: Except for the computer allowance acknowledged above, this study has not received any funding.
- Conflict of interest: The authors declare that they have no conflict of interest.

References

[1] A. Thom, The flow past circular cylinders at low speeds, Proc. R. Soc. Lond. A141 (1933) 651–669.

[2] H. G. Weller, G. Tabor, H. Jasak, C. Fureby, A tensorial approach to computational continuum mechanics using object-oriented techniques, Comp. Phys. 12(6) (1998) 620–631.

[3] D. A. Lysenko, I. S. Ertesvåg, K. E. Rian, Large-eddy simulation of the flow over a circular cylinder at Reynolds number 3900 using the OpenFOAM toolbox, Flow Turbul. Combust. 89 (2012) 491–518.

[4] D. A. Lysenko, I. S. Ertesvåg, K. E. Rian, Large-eddy simulation of the flow over a circular cylinder at Reynolds number 2×10^4, Flow Turbul. Combust. 92 (2014) 673–698.

[5] D. A. Lysenko, I. S. Ertesvåg, Reynolds-averaged, scale-adaptive and large-eddy simulations of premixed bluff-body combustion using the Eddy Dissipation Concept, Flow Turbul. Combust. 100 (2018) 721–768.

[6] A. I. Savitsky, L. N. Schukin, V. G. Karelin, A. M. Mass, R. M. Pushkin, A. P. Shibamov, I. L. Schukin, S. V. Fischenko, Method for controlling boundary layer on an aerodynamic surface of a flying vehicle, United States Patent No. 5417391 (1995).

[7] Z. P. Sluchanovskaya, Pressure distribution on the surface of rectangular, trihedral, and semicircular cylinders and their aerodynamic coefficients (in Russian), Nauchn. Tr. Inst. Mekh. 24 (1973) 52–60.

[8] S. Isaev, P. Baranov, I. Popov, A. Sudakov, A. Usachov, S. Guvernyuk, A. Sinyavin, A. Chylunin, A. Mazo, E. Kalinin, Ensuring safe descend of reusable rocket stages - Numerical simulation and experiments on subsonic turbulent air flow around a semi-circular cylinder at zero angle of attack and moderate Reynolds number, Acta Astronautica 150 (2018) 117–136.

[9] Y. Cao, T. Tamura, Numerical investigations into effects of three-dimensional wake patterns on unsteady aerodynamics characteristics of a circular cylinder at Re= 1.3×10^5, J. Fluids Struct. 59 (2015) 351–369.

[10] E. Robertson, V. Choudhury, S. Bhushana, D. K. Walters, Validation of OpenFOAM numerical methods and turbulence models for incompressible bluff body flows, Comput. Fluids 123 (2015) 122–145.

[11] Y. Cao, T. Tamura, Large-eddy simulations of flow past a square cylinder using structured and unstructured grids, Comput. Fluids 137 (2016) 36–54.

[12] A.-P. Zahiri, E. Roohi, Anisotropic minimum-dissipation (AMD) subgrid-scale model implemented in OpenFOAM: Verification and assessment in single-phase and multi-phase flows, Comput. Fluids 180 (2019) 190–205.

[13] S. Isaev, P. Baranov, I. Popov, A. Sudakov, A. Usachov, S. Guvernyuk, A. Sinyavin, A. Chylunin, A. Mazo, D. Demidov, A. Dekterev, A. Gavrilov, A. Shebelev, Numerical simulation and experiments on turbulent air flow around the semi-circular profile at zero angle of attack and moderate Reynolds number, Comput. Fluids 188 (2019) 1–17.

[14] J. Son, T. Hanratty, Velocity gradients at the wall for flow around a cylinder at Reynolds numbers from 5×10^3 to 10^5, J. Fluid Mech. 35 (1969) 353–368.

[15] A. A. McKillop, F. Durst, A laser anemometry study of separated flow behind a circular cylinder, In Laser anemometry in fluid mechanics II (ed. R. J. Adrian, et al.) LADOAN-IST, Lisbon, Portugal (1986).

[16] L. Ong, J. Wallace, The velocity field of the turbulent very near wake of a circular cylinder, Exp.Fluids. 20 (1996) 441–453.

[17] H. C. Lim, S. J. Lee, Flow control of circular cylinders with longitudinal grooved surfaces, AIAA J. 40(10) (2002) 2027–2036.

[18] P. Parnaudeau, J. Carlier, D. Heitz, E. Lamballais, Experimental and numerical studies of the flow over a circular cylinder at Reynolds number 3900, Phys. Fluids 20(8).

[19] M. Plata, E. Lamballais, F. Naddei, On the performance of a high-order multiscale DG approach to LES at increasing Reynolds number, Comput. Fluids 194 (2019) 104306.

[20] D. F. G. Durao, M. V. Heitor, J. C. F. Pereira, A laser anemometry study of separated flow around a squared obstacle, In Laser anemometry in fluid

mechanics II (ed. R. J. Adrian, et al.) LADOAN-IST, Lisbon, Portugal (1986).

[21] D. Lyn, S. Einav, W. Rodi, J. Park, A laser doppler velocimetry study of ensemble-averaged characteristics of the turbulent near wake of a square cylinder, J. Fluid Mech. 304 (1995) 285–319.

[22] S. Sanquer, P. Bruel, B. Deshaies, Some specific characteristics of turbulence in the reactive wakes of bluff bodies, AIAA J. 36(6) (1998) 994–1001.

[23] M. Minguez, C. Brun, R. Pasquetti, E. Serre, Experimental and high-order LES analysis of the flow in near-wall region of a square cylinder, Int. J. Heat Fluid Flow 32 (2011) 558–566.

[24] F. X. Trias, A. Gorobets, A. Oliva, Turbulent flow around a square cylinder at Reynolds number 22,000: A DNS study, Comput. Fluids 123 (2015) 87–98.

[25] Y. Cao, T. Tamura, H. Kawai, Spanwise resolution requirements for the simulation of high-Reynolds-number flows past a square cylinder, Comput. Fluids 196 (2020) 104320.

[26] B. Geurts, Elements of Direct and Large-Eddy Simulation, R.T.Edwards, Philadelphia (2004).

[27] A. Yoshizawa, Statistical theory for compressible shear flows, with the application to subgrid modelling, Phys. Fluids 29(2152) (1986) 1416–1429.

[28] P. Sagaut, Large Eddy Simulation for Incompressible Flows, 3rd ed., Springer Berlin (2006).

[29] C. Fureby, On subgrid scale modeling in large eddy simulations of compressible fluid flow, Phys. Fluids 8(5) (1996) 1301–1311.

[30] J. P. Vandoormaal, G. D. Raithby, Enhancements of the SIMPLE method for predicting incompressible fluid flows, Numer. Heat Transfer 7 (1984) 147–163.

[31] H. Weller, Controlling the computational modes of the arbitrarily structured c grid, Monthly Weather Rev. 140(10) (2012) 3220–3234.

[32] A. Harten, High resolution schemes for hyperbolic conservation laws, J. Comput. Phys. 49 (1983) 357–393.

[33] C. H. K. Williamson, J. Wu, J. Sheridan, Scaling of streamwise vortices in wakes, Physics Fluids 7(10) (1995) 2307–2309.

[34] B. F. Garcia, G. D. Weymouth, V. T. Nguyen, O. R. Tutty, Span effect on the turbulence nature of flow past a circular cylinder, J. Fluid Mech. 878 (2019) 306–323.

[35] S. Szepesssy, P. W. Bearman, Aspect ratios and end plate effects on vortex shedding from a circular cylinder, J. Fluid Mech. 234 (1992) 191–217.

[36] T. Yamagata, N. Saito, N. Fujisawa, Aeolian tone from a semi-circular cylinder in a stream, J. Flow Control, Measurement Visualization 4 (2016) 30–37.

[37] L. Carassale, A. Freda, M. Marrè-Brunenghi, Experimental investigation on the aerodynamic behavior of square cylinders with rounded corners, J. Fluids Structures 44 (2014) 195–204.

[38] P. Welch, The use of fast fourier transform for the estimation of power spectra: a method based on time averaging over short, modified periodograms, IEEE Trans. Audio Electroacoust. 15(6) (1967) 70–73.

[39] M. Bloor, The transition to turbulence in the wake of a circular cylinder, J. Fluid Mech. 19 (1964) 290–304.

[40] T. Maekawa, S. Mizuno, Flow around the separation point and in the near wake of a circular cylinder, Phys. Fluids (Supp.) (1967) 184–186.

[41] A. Kourta, H. Boisson, P. Chassing, Non-linear interactions and the transition to turbulence in the wake of a circular cylinder, J. Fluid Mech. 181 (1987) 41–161.

[42] C. Norberg, Effects of Reynolds number and a low intensity free stream turbulence on the flow around a circular cylinder, in: Publication No. 87/2, Chalmers University of Technology, Gothenburg, Sweden, 1987.

[43] J. Mihailovic, T. C. Corke, Three-dimensional instability of the shear layer over a circular cylinder, Phys. Fluids 9(11) (1987) 3250–3257.

[44] A. Prasad, C. H. K. Williamson, The instability of the shear layer separating from a bluff body, J. Fluid Mech. 333 (1997) 375–402.

[45] S. Rajagopalan, R. A. Antonia, Flow around a circular cylinder-structure of the near wake shear layer, Exp. Fluids 38 (2005) 393–402.

[46] D. C. Lander, D. M. Moore, C. W. Letchford, M. Amitay, Scaling of square-prism shear layers, J. Fluid Mech. 849 (2018) 1096–1119.

[47] C. Brun, S. Aubrun, T. Goossens, P. H. Ravier, Coherent structures and their frequency signature in the separated shear layer on the sides of a square cylinder, Flow Turbul. Combust 81 (2008) 97–114.

[48] D. M. Moore, C. W. Letchford, M. Amitay, Energetic scales in a bluff body shear layer, J. Fluid Mech. 875 (2019) 543–575.

[49] C. Tropea, A. L. Yarin, J. F. Foss, Springer Handbook of Experimental Fluid Mechanics, Springer, Berlin, Heidelberg (2007).

[50] Y. Nakamura, Y. Ohya, Effects of turbulence on the mean flow past two-dimensional rectangular cylinders, J. Fluid Mech. 149 (1984) 255–273.